Design of graphene-based terahertz metasurface for reconfigurable wavefront manipulations

Tiancheng Zhang(张天成)[1,2], Faqian Chong(种发乾)[1,2], Yulun Wu(吴羽伦)[1,2], Hongsheng Chen(陈红胜)[1,2,3,4,†], and Song Han(韩松)[1,2,‡]

[1] *Innovative Institute of Electromagnetic Information and Electronic Integration, College of Information Science & Electronic Engineering, Zhejiang University (ZJU), Hangzhou* 310027, *China*

[2] *State Key Laboratory of Extreme Photonics and Instrumentation, ZJU-Hangzhou Global Scientific and Technological Innovation Center, Zhejiang University, Hangzhou* 310200, *China*

[3] *International Joint Innovation Center, the Electromagnetics Academy at Zhejiang University, Zhejiang University, Haining* 314400, *China*

[4] *Key Laboratory of Advanced Micro/Nano Electronic Devices & Smart Systems of Zhejiang, Jinhua Institute of Zhejiang University, Zhejiang University, Jinhua* 321099, *China*

(Received 18 September 2025; revised manuscript received 4 November 2025; accepted manuscript online 19 November 2025)

The resonant phase of metasurface, incorporating the geometric phase and propagation phase, has become one of the most effective methodologies to control the electromagnetic wavefronts. In this study, we numerically propose a graphene-based reflective metasurface that employs the resonant phases for terahertz (THz) wavefront control. The metasurface consists of a one-dimensional (1D) graphene grating, a silicon dioxide spacer, and a gold back mirror, which form a Fabry–Perot-type resonant cavity. By tuning the grating width, we achieve precise 0–2π phase control, enabling THz beam deflection and focusing. By further introducing electrical doping to change the Fermi level of the graphene grating, we can realize dynamic phase modulation through a directly applied electrical bias. As a result, the electrically tunable metasurface supports continuously adjustable beam steering and focal lengths without altering its physical structure. These results demonstrate the metasurface's potential for reconfigurable and compact THz photonic devices.

Keywords: graphene metasurface, THz wave manipulation, electrically tunable device

PACS: 78.67.Wj, 42.25.Bs, 42.79.Dj, 78.67.Pt

DOI: 10.1088/1674-1056/ae2114 **CSTR:** 32038.14.CPB.ae2114

1. Introduction

Terahertz (THz) waves, spanning the frequency range of 0.1 THz–10 THz between microwave and infrared bands, have attracted increasing attention due to their immense potential in applications such as wireless communications, imaging, and spectroscopy.[1] However, the efficient control and manipulation of THz waves remain a significant challenge due to the lack of standard optical components. Metamaterials, as artificially designed materials with special electromagnetic (EM) properties,[2–5] have gradually become one of the most important research directions due to their excellent ability to manipulate THz waves. In particular, metasurfaces, as two-dimensional (2D) metamaterials, have become a hotspot in research because of their unique characteristics.[6–10] By designing subwavelength-scale planar structures, metasurfaces can effectively control the phase, amplitude, or polarization of EM waves, thereby enabling precise manipulation of THz waves.[11] Based on this property, many THz devices based on metasurfaces have been proposed, such as metalenses,[12–15] vortex beam generators,[16–18] and beam deflectors.[19,20]

Although conventional metasurfaces have demonstrated various physical effects in THz manipulation, most of them are based on static designs. That is, once the devices are fabricated, their EM responses are fixed, making them unsuitable for dynamic control applications. In recent years, tunability and reconfigurability have emerged as research hotspots. These approaches rely on integrating stimuli-responsive materials to enable real-time modulation of the metasurface responses.[21–25]

Several studies have explored materials such as GaAs, VO_2, and 2D electron gas (2DEG) to dynamically alter their dielectric constants or conductivities under external stimuli like electric fields, thermal excitation, or optical pumping.[26] For instance, VO_2 can switch between metallic and insulating phases, modulating THz transmission and reflection upon thermal or optical activation.[27–31] Similarly, 2DEG structures, known for their high carrier mobility, enable GHz-scale modulation speeds through their gate voltage control of resonance strength.[32] Nonetheless, these materials often suffer from limitations such as slow response times, high losses, or complex integration, hindering their application in high-speed communication and compact optoelectronic systems.

In contrast, graphene, as the first successfully isolated

†Corresponding author. E-mail: hansomchen@zju.edu.cn

‡Corresponding author. E-mail: song.han@zju.edu.cn

© 2026 Chinese Physical Society and IOP Publishing Ltd. All rights, including for text and data mining, AI training, and similar technologies, are reserved.

CPB Online Press

2D material, exhibits exceptionally high carrier mobility ($>10^4$ cm^2/V·s)[33] and tunable surface conductivity, making it a naturally well-suited candidate for THz plasmonic applications.[34–36] By applying a gate voltage, the motion of free carriers in graphene can be efficiently modulated, thereby tuning its chemical potential and surface conductivity. Unlike materials such as VO_2 or GaAs that rely on discrete phase transitions, graphene enables continuous and reversible conductivity modulation through electrostatic gating or chemical doping, allowing fine and real-time control of the reflection amplitude and phase without altering the device geometry. Thanks to its ultrafast carrier dynamics, graphene exhibits picosecond–nanosecond response under gate bias, greatly enhancing the real-time tunability of THz metasurfaces. Consequently, graphene-based metasurfaces combine low-loss plasmonic behavior,[37,38] broadband continuous tunability, and ultrafast electrical response, providing an ideal platform for high-speed and reconfigurable THz wave control.[39–43]

In this work, we propose a tunable reflective metasurface based on a 1D graphene grating structure. The design features a Fabry–Perot-type cavity configuration where the front graphene grating acts as a semi-reflective mirror, the back metal mirror ensures high reflectivity, and a silicon dioxide layer fills the cavity to enable resonance. By tuning the grating width, precise control over the reflection phase is achieved, allowing the construction of static devices such as a metalens and a beam deflector. Furthermore, we demonstrate a dynamic electrically tunable approach by modulating the Fermi level of graphene through gate voltage, enabling functionalities such as a varifocal lens and a reconfigurable beam modulator. Simulation results confirm that the metasurface achieves a reflection phase modulation range approaching 2π with high reflectivity, validating its superior performance and potential for applications in THz communication and imaging.

2. Design of graphene-based THz metasurface

2.1. Design of the metasurface

Figure 1(a) shows the graphene-based metasurface design, where the unit cell structure comprises a front semi-reflective mirror formed by a 1D graphene grating, a back mirror made of highly reflective gold, and a middle dielectric layer of silicon dioxide acting as the resonant cavity. The Fermi level of the graphene grating can be mediated by electrical doping such that the graphene grating exhibits metal-like optical properties for plasmonic resonance in the THz frequency range, as shown in Fig. 1(b). The resonant phase covering the 0–2π range can be obtained when the x-polarized THz wave is incident on the metasurface. In this work, the proposed device is primarily designed for the manipulation of transverse magnetic (TM) polarized THz waves, where the electric field is perpendicular to the graphene grating strips (along the x-axis).

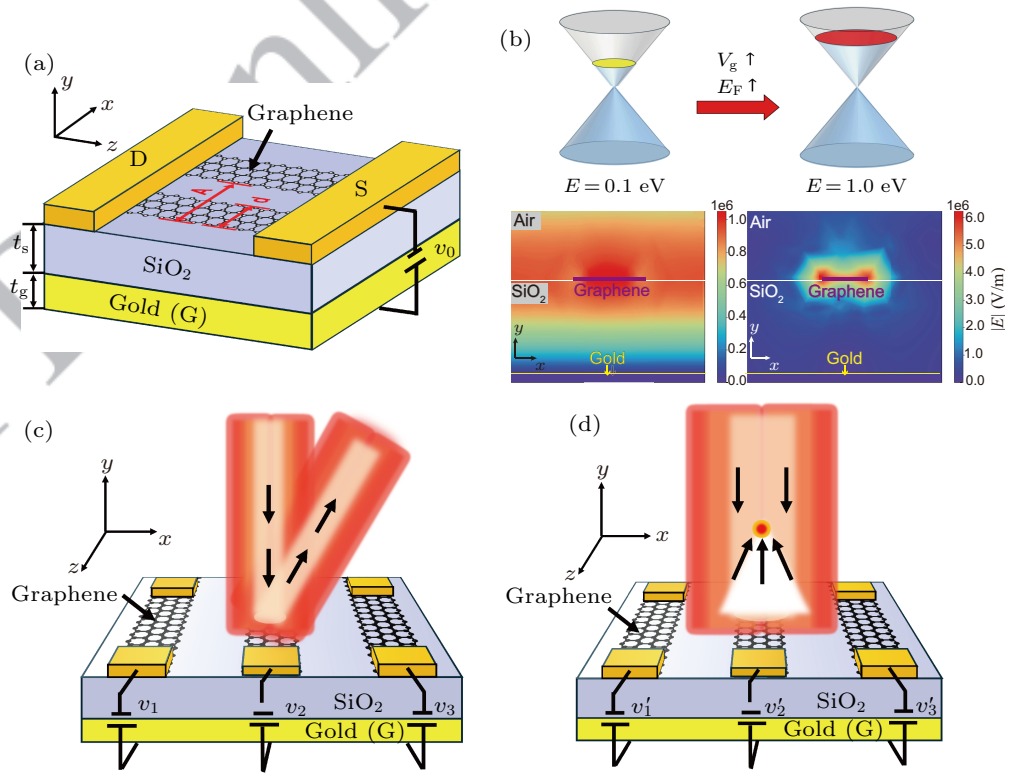


Fig. 1. Schematic diagram of the electrically tunable graphene metasurface and its modulation mechanism. (a) Perspective view of a graphene grating structure composed of two unit cells, where $t_s = 6.3$ μm, $t_g = 0.5$ μm, $A = 16$ μm. (b) Fermi level tuning via applied gate voltage at an operating frequency of 8 THz, enabling dynamic modulation of the graphene surface conductivity; bottom panels show simulated electric field distributions of a unit cell at different Fermi levels. (c) Electrically controlled beam deflector based on phase gradient engineering. (d) Electrically tunable metalens achieving dynamic focal tuning via spatially varying gate voltages.

CPB Online In-Press

Two main strategies can be employed to design graphene-based THz metasurfaces. First, periodically arranged graphene gratings can be uniformly biased by the same voltage, *i.e.*, equalizing the Fermi level, as shown in Fig. 1(a). To realize THz functional devices like a beam deflector or a metalens, the geometric parameters, *e.g.*, the width of graphene gratings or the unit cell period, can be manipulated and artificially arranged. Alternatively, the graphene gratings can be uniformly distributed but each grating can be biased independently by artificially coded voltages. As a result, a THz beam deflector or a metalens can be further designed with reconfigurable characteristics, as shown in Figs. 1(c) and 1(d), respectively.

From a fabrication perspective, the proposed metasurface can be realized using conventional micro/nano-fabrication techniques. Single-layer graphene can be grown using a copper-catalyzed chemical vapor deposition (CVD) approach in a quartz tube furnace with CH_4 and H_2 as precursors. After growth, graphene sheets larger than 1 cm^2 can be transferred onto the SiO_2 substrate using a PMMA-assisted wet-etch method to remove the copper catalyst.[44,45] Finally, the graphene can be patterned into a one-dimensional grating using standard photolithography followed by oxygen plasma etching. This fabrication route is fully compatible with current CMOS processes and has been widely demonstrated in graphene-based metasurface research.

2.2. Graphene optical properties in the THz range

Graphene is a unique 2D dispersive material exhibiting strongly frequency-dependent electrical responses in the THz regime. Its surface conductivity is typically described using the Kubo formalism. Under the random phase approximation (RPA),[46,47] the conductivity can be simplified as a combination of intraband and interband contributions, both expressed as functions of the angular frequency:

$$\sigma_{\text{intra}}(\omega) = \frac{e^2 k_B T \tau}{\pi\hbar^2 (1 - \mathrm{i}\omega\tau)} \left[\frac{\mu_c}{k_B T} + 2\ln \times \left(\exp\left(-\frac{\mu_c}{k_B T} \right) + 1 \right) \right], \tag{1}$$

$$\sigma_{\text{inter}}(\omega) = \frac{\mathrm{i}e^2}{4\pi\hbar} \ln \left[\frac{2|\mu_c| - (\omega + \mathrm{i}\tau^{-1})\hbar}{2|\mu_c| + (\omega + \mathrm{i}\tau^{-1})\hbar} \right], \tag{2}$$

where τ denotes the electron relaxation time, μ_c represents the chemical potential of graphene, e is the electron charge, T is the temperature, k_B stands for Boltzmann's constant, and $\hbar$ indicates the reduced Planck constant.

Since the interband conductivity primarily originates from electron transitions across the Dirac point, such transitions can only occur when the incident photon energy exceeds twice the chemical potential. Therefore, in the THz range and for $\mu_c \geq 0.1$ eV, the interband contribution becomes negligible. In this case, the total surface conductivity is dominated by the intraband term, which closely follows the Drude model, similar to that of noble metals. As a consequence, we mainly adopt the intraband conductivity (*i.e.*, Eq. (1)) in this work. It is also worth mentioning that the chemical potential (Fermi level) of graphene can be dynamically tuned by applying external gate voltages. When a positive gate voltage is applied, the carrier concentration in graphene increases, progressively filling the Dirac cone and thereby raising the Fermi level and leading to the variation of graphene's surface conductivity.[48] This property is employed to design reconfigurable electronic and EM devices. In monolayer graphene, the relationship between the gate voltage V_g, carrier concentration n, and Fermi level E_F can be described as follows:

$$E_F = \hbar v_F \sqrt{\pi |n|}, \tag{3}$$

$$n = \frac{C_g (V_g - V_{\text{Dirac}})}{e}, \tag{4}$$

where v_F is the Fermi velocity, C_g is the gate capacitance per unit area, V_{Dirac} is the Dirac point voltage, and e is the elementary charge. These expressions indicate that the Fermi level is proportional to the square root of the gate voltage deviation from the Dirac point.

By considering an effective graphene thickness of $h_{\text{eff}} = 1$ nm, the corresponding linear relative permittivity is given by[49]

$$\varepsilon(\omega) = 1 + \frac{\mathrm{i}\sigma_s}{\varepsilon_0 \omega h_{\text{eff}}}. \tag{5}$$

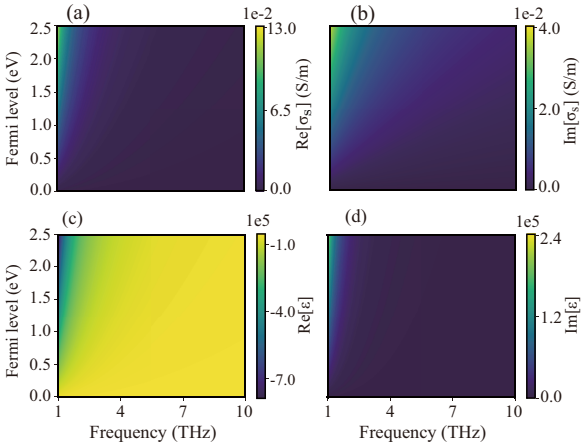


Fig. 2. (a)–(b) Graphene surface conductivity as a function of Fermi level and frequency. (c)–(d) Dependence of graphene's permittivity on Fermi energy and frequency.

Figure 2 illustrates how the surface conductivity and permittivity of graphene vary with frequency and Fermi level, thereby validating its tunable EM properties under different bias conditions. In all numerical simulations, unless otherwise specified, the carrier relaxation time is set to $\tau = 0.5$ ps and the temperature to $T = 300$ K. The refractive index of the silicon dioxide spacer is fixed at 1.5, while the gold back mirror

CPB Online In-Press

is modeled as a perfect electric conductor (PEC). The incident wave is transverse-magnetic (TM) polarized and normally incident onto the metasurface.

3. Static graphene metasurfaces

3.1. Analysis of reflectance and phase

To investigate the phase modulation capability of the graphene-based metasurface, the width of the graphene grating is varied by using the finite element method in the commercial software COMSOL Multiphysics. The metasurface structure was modeled according to the design described in Fig. 1, where the periodic boundary condition was applied along the x-axis. The transition boundary is adopted to depict the graphene with the corresponding surface conductivity defined via the Drude formula, capturing its frequency-dependent electromagnetic response. The back reflector was modeled as a perfect electric conductor (PEC) to approximate an ideal high-reflectivity gold mirror, and the refractive index of the intermediate silicon dioxide layer was set to 1.5. With graphene's Fermi level fixed at 1.2 eV, a parametric sweep was conducted over both frequency and grating width to examine the reflection characteristics of the metasurface. The resulting reflection amplitude and phase distributions as functions of frequency and grating width are shown in Fig. 3. When the grating width exceeds approximately 12 μm, a higher-order resonance is excited inside the cavity, resulting in a noticeable decrease in reflectance. However, such unit cells are not employed in our metasurface design. In practice, only elements with width < 12 μm are selected, where the reflection amplitude stays above 0.5. Based on these selected unit cells, we calculated the overall efficiency of the metasurface by taking the arithmetic mean of the reflectance values, yielding an efficiency of approximately 82.3% at 8 THz.

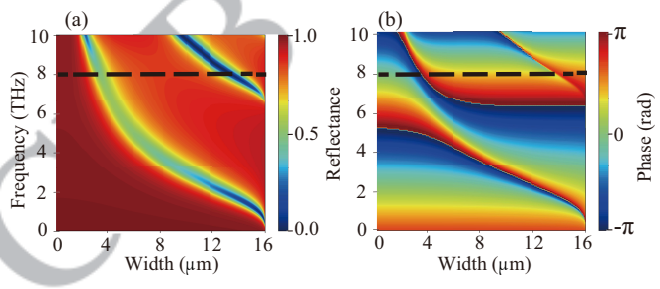


Fig. 3. (a) Reflection amplitude and (b) phase variation as functions of frequency and grating width at a fixed Fermi level of 1.2 eV. The dashed line indicates the operating frequency of 8 THz. A noticeable drop in reflection amplitude occurs around a grating width of 13 μm, which is attributed to the excitation of higher-order resonances. In this work, all unit-cell designs employ grating widths below 12 μm; the range is extended to 16 μm here only for consistency with the subsequent figures.

The simulation results provide a database for both phase range and reflection efficiency that allows us to design resonant-phase-modulated metasurfaces for THz wavefront control. For example, at a frequency of 8 THz, the achievable phase coverage reaches up to $(5/3)\pi$ and the reflectance remains above 0.5 by simply varying the grating width, as shown in Fig. 3. Therefore, the actual device can be designed by solely changing the grating width of the graphene, which may also facilitate the real device fabrication.

3.2. THz beam deflector

We first demonstrate a beam-bending metasurface device, as shown in Fig. 4. The underlying principle is governed by the generalized Snell's law[20]

$$\sin(\theta_r) - \sin(\theta_i) = \frac{\lambda}{2\pi \cdot n_i} \cdot \frac{d\varphi}{dx}, \tag{6}$$

where n_i denotes the refractive index of the incident medium, $d\varphi/dx$ is the phase gradient at the interface between two media, and λ stands for the wavelength of the incoming THz wave. The angles of incidence and reflection are denoted by θ_i and θ_r, respectively. When the incidence is normal and $n_i = 1$ (air), the corresponding reflection angle can be determined by

$$\theta_r = \sin^{-1}\left(\frac{\lambda}{2\pi} \cdot \frac{d\varphi}{dx}\right). \tag{7}$$

In our numerical simulation, the device containing 84 graphene gratings was designed and arranged, where widths were carefully chosen such that the phase difference between adjacent units was maintained at $\pi/3$. For the designed device in this configuration, every six units form a complete array with a total phase coverage of 2π. Therefore, the 84 units correspond to 14 repeated arrays. The required grating width of each grating is selected based on the phase–width relationship shown in Fig. 3.

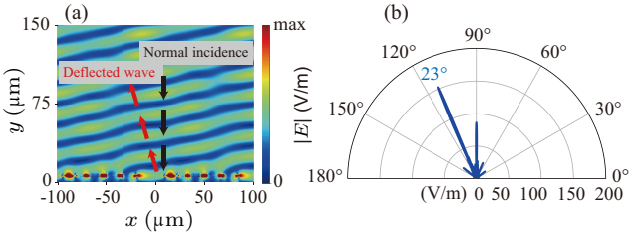


Fig. 4. (a) Electric field distribution of the reflected wave at an incident frequency of 8 THz, showing a tilted wavefront indicative of beam deflection; (b) corresponding far-field radiation pattern. The main lobe is deflected at an angle of 23.0°, in agreement with the prediction from the generalized Snell's law. The strong zero-order reflection is mainly due to the intense reflection from the gold substrate.

Figure 4 shows the simulated electric field distribution of the reflected wave and the corresponding far-field radiation pattern, where the deflection direction with maximum energy intensity is clearly observed. The numerically simulated deflection angle matches well with the theoretical value, confirming the effectiveness of the beam deflector design. Under normal incidence at a frequency of 8 THz, the simulation results clearly show that the wavefront is deflected with a bending angle around 23°, which is consistent with the prediction from the generalized Snell's law. It should be noted that Fig. 4 clearly exhibits a strong zero-order reflection, primarily

CPB Online In-Press

due to the intense specular reflection from the gold substrate. The deflection efficiency, defined as the ratio of the first-order diffraction power to the total reflected power, is calculated to be 30.4% at 8 THz for the structure.

3.3. THz metalens

The metalens is another typical device that requires phase manipulation of EM waves. To obtain a graphene-based metalens with a single focal point, it is essential to design the reflected waves from each resonant grating that arrive at the focal point with identical phase. For a given focal length F, the phase profile at the reflective interface must satisfy the following expression:

$$\varphi(x) = \frac{2\pi}{\lambda}\left(\sqrt{F^2+x^2} - F\right). \tag{8}$$

In this design, the Fermi level is fixed as 1.2 eV, and phase modulation is achieved by varying the grating width of each unit cell. However, since the attainable phase range does not fully cover 2π, a modified phase distribution strategy is employed. Specifically, we design a realizable phase profile by focusing on maintaining appropriate phase differences between adjacent unit cells. In such a design, the focal length is chosen as $F = 400$ μm, and the transverse coordinate is discretized as $x = mA$, where A is the unit cell period and $m = \pm 1$, ± 2, …, ± 22. Based on the grating resonant phase–width relationship provided in Fig. 3, the corresponding discrete phase distribution as a function of x is plotted in Fig. 5(a).

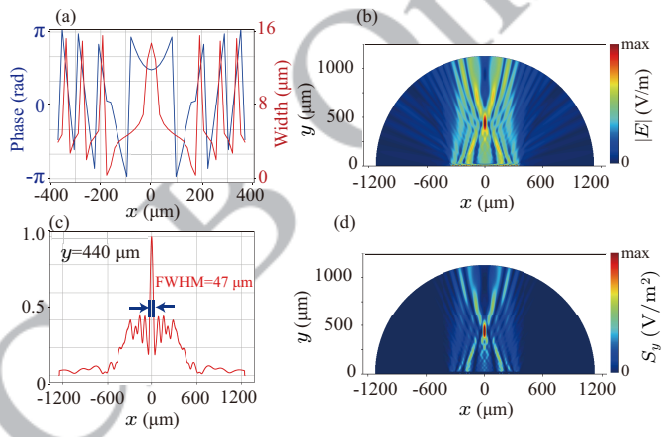


Fig. 5. (a) Grating width and corresponding reflection phase distribution as a function of transverse position x; (b) simulated electric field magnitude of the reflected wave, showing single-point focusing behavior under normal incidence; (c) normalized reflected field intensity along the focal plane at $y = 440$ μm, where the full width at half maximum (FWHM) is measured to be 47 μm, demonstrating effective focusing performance; (d) time-averaged Poynting vector distribution, indicating energy convergence at the focal point.

As shown in Figs. 5(b) and 5(d), the designed metalens exhibits a clear focusing behavior under normal incidence at 8 THz, where the focal spot is located at approximately $y = 440$ μm. The deviation from the designed focal length is primarily attributed to the finite size of the unit cells and the phase discontinuities caused by the limited phase coverage. The normalized field intensity profile along the x-axis at the focal plane is plotted in Fig. 5(c). The full width at half maximum (FWHM) is measured to be 47 μm, and the focusing efficiency of the metalens is 30.8%.

The efficiency reduction arises from phase discretization among adjacent elements and partial reflection losses due to impedance mismatch between the graphene surface and the dielectric layer.

4. Electrically reconfigurable graphene metasurfaces

4.1. Analysis of reflectance and phase

Since the graphene metasurface designed based on grating width is inherently static, it may not be able to meet the practical demands for tunable devices. Since practical terahertz metasurface devices require tunability and reconfigurability, static structures are often insufficient to meet application demands. Graphene, however, offers an effective solution: by varying the applied gate voltage, we can modulate the carrier density, which in turn shifts the Fermi level and alters the surface conductivity. This intrinsic electrical tunability makes graphene highly adaptable to the requirements of dynamic THz control. Therefore, we further investigated its electro-modulation characteristics. To address this limitation, we further investigated the structure's electrical tunability. Given that the gate voltage directly affects the Fermi level of graphene and thereby modulates its surface conductivity, we simulated the variation in gate bias by adjusting the Fermi level, in order to evaluate the dynamic tunability of the reflected wave under fixed grating width conditions.

Through parameter sweeps, we fixed the grating width at 2.875 μm. The reflection phase and amplitude were then analyzed as functions of the Fermi level across different frequencies. As shown in Fig. 6, at an incident frequency of 8 THz, the reflection phase achieves a tunable range of up to $(11/6)\pi$, while the reflectance remains above 0.35. This result demonstrates a superior phase tuning capability compared to the static metasurface structure based solely on grating width variation.

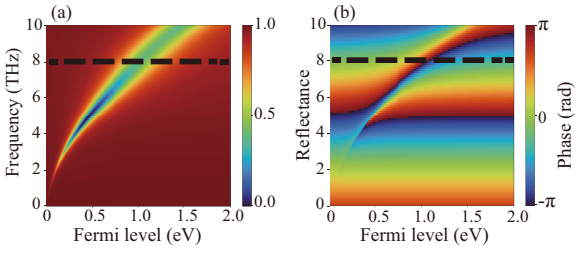


Fig. 6. (a) Reflection amplitude *versus* frequency and Fermi level, (b) reflection phase *versus* frequency and Fermi level. Grating width is fixed at 2.875 μm; dashed line marks 8 THz.

Online In-Press

4.2. THz reconfigurable beam deflector

To validate the practical effectiveness of the proposed electrically tunable graphene unit structure in beam steering applications, we conducted a series of simulations based on the generalized Snell's law. By dynamically modulating the phase profile of the unit cells via Fermi level adjustment, we achieved continuous tuning of the reflection angle under normal incidence at 8 THz.

Specifically, the beam deflector consists of 132 unit cells, which are divided into different arrays according to the design requirements, with each array covering a full 2π phase range. When the phase gradients were set to the following values $\pi/6$, $\pi/3$, $\pi/2$, and $2\pi/3$, the corresponding numbers of unit cells in each array are 11, 6, 4, and 3, respectively. Following this design principle and as illustrated in Fig. 6, the Fermi level of each unit cell was adjusted to satisfy the required phase distribution, and numerical simulations were subsequently performed. The simulation results, which include the electric field distributions and corresponding far-field patterns for various tuning states (as shown in Fig. 7), demonstrate that the reflected beam can be continuously steered over a wide angular range from 11.1° to 51.2°, confirming the strong tunability of the proposed structure. As the phase gradient increases, the deflection efficiencies are 33.3%, 31.0%, 29.7%, and 27.4%, respectively. The gradual decrease in efficiency is mainly attributed to the enhanced phase gradient that increases diffraction into higher-order modes, as well as the intrinsic impedance mismatch between the graphene sheet and the dielectric spacer.

It is worth noting that in this work, we only simulated phase profiles with monotonically increasing phase along the x-axis. However, by inverting the phase gradient (*i.e.*, decreasing phase along the x-axis), the reflection direction can be symmetrically reversed, offering an extended degree of control.

A comparison between the simulated deflection angles and theoretical predictions reveals an angular error of less than 0.1° in all cases. This excellent agreement confirms the high precision and robustness of the proposed device for manipulating reflected THz waves, thereby validating its feasibility and potential for practical implementation as an electrically tunable beam deflector.

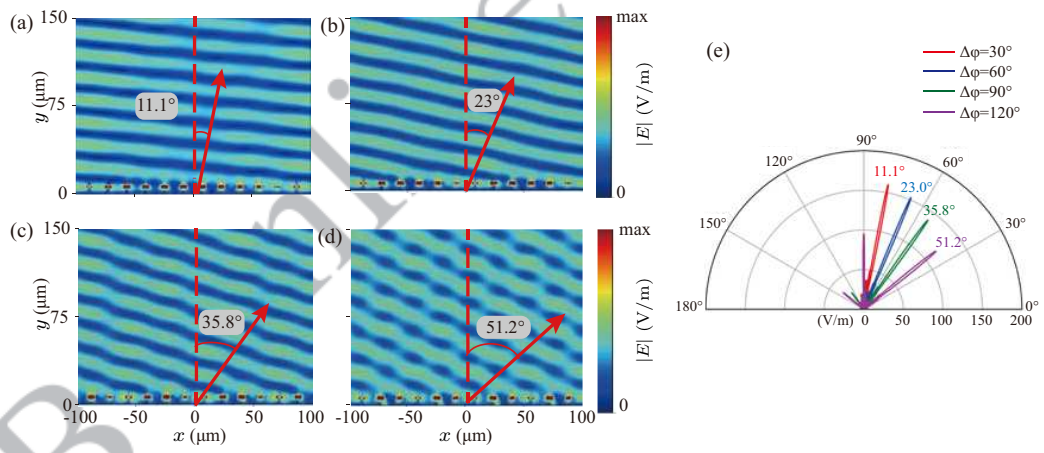


Fig. 7. Reflected electric field distributions and far-field deflection angles under different phase gradients: Panels (a)–(d) correspond to $\Delta\varphi = \pi/6$, $\pi/3$, $\pi/2$, $2\pi/3$, respectively; (e) far-field deflection angles as a function of phase gradient, demonstrating continuous tunability of the device. In each case, a certain portion of the reflected wave remains in the zeroth-order direction, with the calculated deflection efficiencies being 33.3%, 31.0%, 29.7%, and 27.4%, respectively.

4.3. THz reconfigurable metalens

To further demonstrate the flexibility and practical potential of the proposed electrical tuning strategy, we designed an electrically focus-tunable metalens. By dynamically adjusting the Fermi level of the graphene unit cells, the focal position can be reconfigured in real time. The device consists of 87 unit cells in total, including one central unit and 43 units on each side, where the phase distributions of the left and right units are designed symmetrically. The Fermi level of each unit is determined according to the ideal phase distribution function described in Eq. (8). Based on the target focal length F, the corresponding reflection phase profile is constructed, and the Fermi levels of the unit cells are tuned to match the desired phase response.

Under normal incidence at 8 THz, we configured four metalens designs with focal lengths of 200 μm, 400 μm, 600 μm, and 800 μm. The simulated results are presented in Fig. 8. Figure 8(a) displays the theoretical phase profiles (blue curves) and the corresponding Fermi level distributions (red curves) as functions of the transverse position x. We adjusted the Fermi level of each unit cell to satisfy the prescribed phase distribution and carried out numerical simulations accordingly. The resulting reflected electric field distributions and the time-averaged Poynting vectors for the four focal configurations are

presented in Figs. 8(b) and 8(c), respectively. All cases clearly exhibit focusing behavior at their respective target positions. Despite the variation in phase profiles across different focal lengths, accurate phase matching is achieved through appropriate Fermi level modulation, enabling effective control over the focal spot location.

Figure 8(d) presents the normalized intensity profiles along the focal plane for each case. The full width at half maximum (FWHM) of the focused beams is 20 μm, 47 μm, 65 μm, and 87 μm, and the focusing efficiencies for the four focal lengths are 26.7%, 34.5%, 33.4%, and 32.0%, respectively, demonstrating strong focusing performance across the entire zoom range. A slight deviation is observed in the 800 μm case, which can be attributed to phase discretization errors caused by the limited number of unit cells. Nevertheless, the overall accuracy remains high.

These results confirm that by electrically tuning the Fermi levels of individual unit cells, real-time focal length adjustment can be achieved, paving the way for ultrathin, reconfigurable, and integrable planar optical devices.

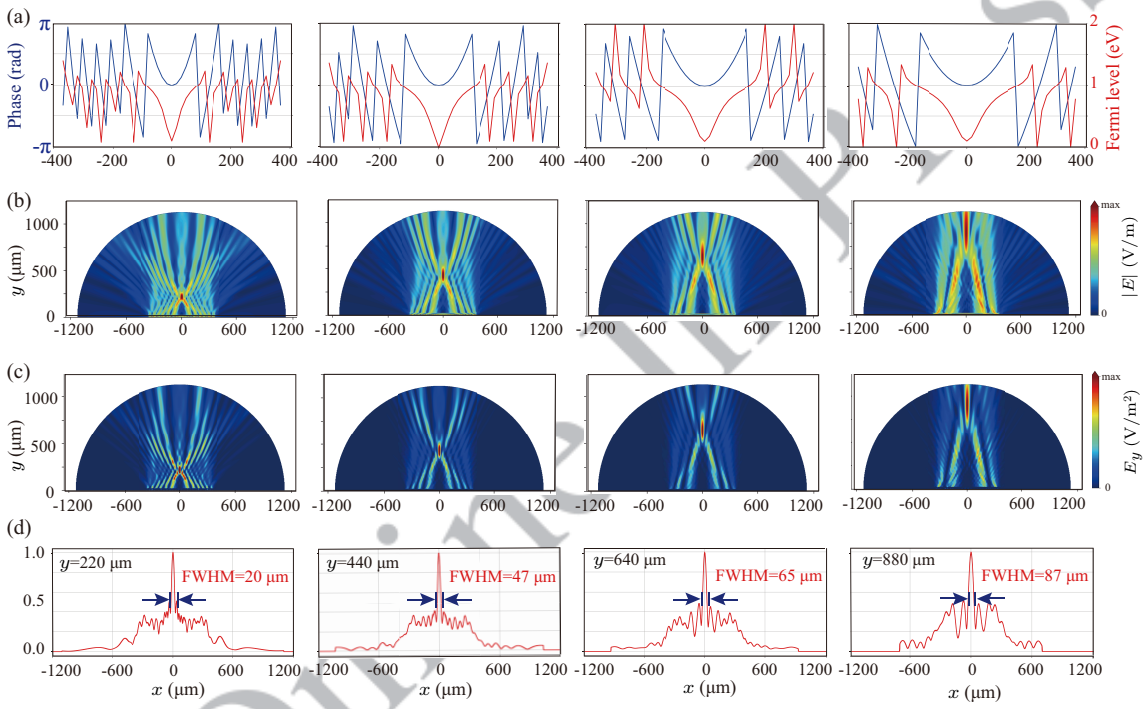


Fig. 8. Simulated results of the electrically tunable-focus metalens at different focal lengths: (a) reflection phase (blue) and required Fermi level (red) as functions of position x; (b) reflected electric field distributions ($|E|$); (c) time-averaged Poynting vector distributions (S_y); (d) normalized intensity profiles along the focal plane with corresponding FWHM. The results confirm that dynamic tuning of the Fermi level enables continuous focal length modulation from 200 μm to 800 μm under 8-THz normal incidence.

5. Conclusion

In this work, we designed and simulated a graphene-based reflective metasurface capable of both static and dynamic phase modulation in the THz regime. By tuning the grating width and the Fermi level of graphene, we enabled two types of functionalities, including fixed-structure beam deflection and metalensing, as well as electrically tunable beam steering and focal length adjustment. The metasurface exhibits high reflectance and a phase tuning range close to 2π, with deflection angle errors within 0.1°, confirming its precise wavefront control capabilities. Moreover, although the present metasurface achieves 1D phase modulation along the x-direction, this concept can be naturally extended to 2D wavefront control. By integrating two orthogonal graphene strip gratings within each unit cell and introducing a thin insulating layer (such as SiO_2) between them to ensure electrical isolation, independent bias tuning of the two graphene strips can be realized. This configuration enables dynamic and fully independent modulation of the reflected THz phase in both dimensions. Consequently, such a 2D extension offers greater flexibility and can support advanced functionalities, including vortex beam generation, dynamic holography, and polarization-dependent wavefront engineering. We believe that the proposed electrically tunable graphene metasurface offers a robust foundation for developing next-generation reconfigurable THz photonic devices.

Acknowledgements

Project supported by the National Key Research and Development Program of China (Grant No. 2024YFB2808200), the National Natural Science Foundation of China (Grant No. 62475230), the Excellent Young Scientists Fund Program (Overseas) of China, and the Fundamental Research Funds for the Central Universities.

CPB Quantum Press

References

[1] Tonouchi M 2007 *Nat. Photon.* **1** 97
[2] Smith D, Pendry J and Wiltshire M 2004 *Science* **305** 788
[3] Soukoulis C M and Wegener M 2011 *Nat. Photon.* **5** 523
[4] Liu Y and Zhang X 2011 *Chem. Soc. Rev.* **40** 2494
[5] Cai W and Shalaev V M 2010 *Optical Metamaterials: Fundamentals and Applications* (New York: Springer)
[6] Kildishev A V, Boltasseva A and Shalaev V M 2013 *Science* **339** 1232009
[7] Yu N and Capasso F 2014 *Nat. Mater.* **13** 139
[8] Yao K and Liu Y 2014 *Nanotech. Rev.* **3** 177
[9] Zhang Y J, Li C L, Luan J Q, Zhao M, Gao D S and Li P L 2024 *Chin. Phys. B* **33** 104210
[10] Prasad N, Pardhasaradhi P, Madhav B T P, Ramakrishna Y and Hasitha Y A 2023 *Prog. Electromagn. Res. M* **117** 119
[11] He Z, Wang H, Cui Z, Xia S, Tang X, Zheng B, Lin X, Shen L, Chen H and Wu Y 2024 *Prog. Electromagn. Res.* **181** 1
[12] Aieta F, Genevet P, Kats M A, Yu N, Blanchard R, Gaburro Z and Capasso F 2012 *Nano Lett.* **12** 4932
[13] Chen X, *et al*. 2012 *Nat. Commun.* **3** 1198
[14] Padilla W J and Averitt R D 2022 *Nat. Rev. Phys.* **4** 85
[15] Wang Y, Zou H Y, Lu Y J, Gu S, Qian J, Xia J P, Ge Y, Sun H X, Yuan S Q and Liu X J 2023 *Prog. Electromagn. Res.* **177** 127
[16] Khorasaninejad M, *et al*. 2016 *Science* **352** 1190
[17] Mei F, Qu G, Sha X, *et al*. 2023 *Nat. Commun.* **14** 6410
[18] Mehmood M Q, Mei S, Hussain S, Huang K, Siew S Y, Zhang L, *et al*. 2016 *Adv. Mater.* **28** 2533
[19] Yue F, Wen D, Zhang C, Gerardot B D, Wang W, Zhang S, *et al*. 2017 *Adv. Mater.* **29** 1603838
[20] Yu N, *et al*. 2011 *Science* **334** 333
[21] Ni X, Emani N K, Kildishev A V, Boltasseva A and Shalaev V M 2012 *Science* **335** 427
[22] Lin P, Qian C, Zhang J, Chen J, Zhu X, Wang Z, Huangfu J and Chen H 2023 *Prog. Electromagn. Res.* **178** 83
[23] Liu C, Li Y, Huang F, Xu G, Li Q, Wang S, Xu Q, Gu J and Han J 2024 *Prog. Electromagn. Res.* **181** 21
[24] Shi Y, Xu X Y, Wang S Z, Wei W Y and Wu Q W 2024 *Chin. Phys. B* **33** 014201
[25] Bai X, Tan S, Mikki S, Li E and Cui T J 2024 *Prog. Electromagn. Res.* **179** 1
[26] Yoon H, Yeung K Y, Kim P and Ham D 2014 *Phil. Trans. R. Soc. A Math. Phys. Eng. Sci.* **372** 20130104
[27] Liu M, Hwang H, Tao H, *et al*. 2012 *Nature* **487** 345
[28] Pashkin A, Kübler C, Ehrke H, Lopez R, Halabica A, Haglund R F, Huber R and Leitenstorfer A 2011 *Phys. Rev. B* **83** 195120
[29] Lee D, *et al*. 2018 *Science* **362** 1037
[30] Yan D X, Feng Q Y, Yuan Z W, Meng M, Li X J, Qiu G H and Li J N 2022 *Chin. Phys. B* **31** 014211
[31] Li J S and Li Z W 2022 *Chin. Phys. B* **31** 094201
[32] Singh P and Sonkusale S 2017 *Sci. Rep.* **7** 40933
[33] Gosling J H, Makarovsky O, Wang F, *et al*. 2021 *Commun. Phys.* **4** 30
[34] Novoselov K S, *et al*. 2004 *Science* **306** 666
[35] Novoselov K, *et al*. 2005 *Proc. Natl. Acad. Sci. USA* **102** 10451
[36] Wang C, Tan S, Lin X, Chen H and Gao F 2023 *Prog. Electromagn. Res.* **177** 85
[37] In C, Kim U J and Choi H 2022 *Light Sci. Appl.* **11** 313
[38] Deng L, *et al*. 2017 *Sci. Rep.* **7** 10558
[39] Jin L, Xie J, Pan B and Luo G 2023 *Prog. Electromagn. Res.* **178** 103
[40] Yang J L, Liu K W and Shen D Z 2017 *Chin. Phys. B* **26** 047308
[41] Squires A D, Gao X, Du J, *et al*. 2022 *Commun. Mater.* **3** 56
[42] Khajeh A, Hamzavi-Zarghani Z, Yahaghi A, *et al*. 2021 *Sci. Rep.* **11** 1296
[43] Qureshi U U R, Basir S, Mallek F, *et al*. 2024 *Sci. Rep.* **14** 5118
[44] Li X, *et al*. 2009 *Science* **324** 1312
[45] Sensale-Rodriguez B, Yan R, Kelly M, *et al*. 2012 *Nat. Commun.* **3** 780
[46] Hanson G W 2008 *J. Appl. Phys.* **103** 064302
[47] Wang D W, Zhao W S, Gu X Q, Chen W C and Yin W Y 2015 *IEEE Trans. Nanotechnol.* **14** 250
[48] Avetisyan A A, Partoens B and Peeters F M 2009 *Phys. Rev. B* **80** 195401
[49] You J W, Threlfall E, Gallagher D F G and Panoiu N C 2018 *J. Opt. Soc. Am. B* **35** 2754

CPB Online in Press